

Investigation of the integrated fuel cell, battery, and heat pump energy systems

Nan Zhang, Yiji Lu^{*,1}, Sambhaji Kadam, Zhibin Yu¹

James Watt School of Engineering, University of Glasgow, Glasgow G12 8QQ, UK

ARTICLE INFO

Keywords:

Integrated FCBEV
Heat pump
Fuel cell
Advanced thermal management
Battery

ABSTRACT

The integration of an advanced fuel cell battery electric vehicle was proposed to extend the driving range, increase the overall energy efficiency, and produce an additional cabin space heating service for on-board vehicle application in winter. The adopted heat pump absorbs heat from the fuel cell and battery during charging and discharging scenarios at the heat pump's cold end and transfers it to the cabin supply air for cabin heating. A numerical model for the proposed system was developed and validated by published experimental results. A comprehensive evaluation of the influence of fuel cell output current, battery discharging rate, ambient air temperature, evaporator coolant inlet temperature and refrigerant subcooling degree on the Coefficient of Performance (COP), outlet air temperature, and Equivalent Effective Battery Capacity (EEBC) were conducted. In addition, in this study, a detailed comparison of proposed system to previously published existing systems was carried out in terms of COP, heating capacity, EEBC, and operating price in order to examine the advantages of the proposed system. Results showed that the proposed system was not sensitive to ambient air temperature, but evaporator coolant inlet temperature had the greatest impact on COP, compared to other defined independent variables. A maximum COP of 6.07 could be observed when the evaporator coolant inlet temperature was 32 °C. Although increasing fuel cell output current and battery discharging rate could increase heating capacity, it would decrease outlet air temperature as well. The price of a single charging cycle for running for a 4-hour period was estimated. Compared to conventional Electric Vehicle Air Source Heat Pump (EVASHP) system and Positive Temperature Coefficient (PTC) heaters, the proposed system has the lowest cost which was £10.40 per charging cycle while the others are £13.8 and £19.2 respectively when providing the same EEBC and heating capacity. Additionally, the payback period was 10,500 charging cycles. Overall, this study provides a potential solution for efficient cabin heating of electric vehicles in extremely cold weather with twice the EEBC of the existing EVASHP system and with 2.8 times of a PTC system both at -20 °C and the operating price is also 1/3 lower than the existing EVASHP. Meanwhile, the COP of the proposed system is 2.3 times that of the existing systems. It can sufficiently increase the driving range of electrical vehicles in winter and eliminate driving range anxiety.

1. Introduction

Conventional internal combustion engine vehicles (ICEVs) significantly changed the way people live and the quality of life. However, the pollution and CO₂ emissions caused by vehicles cannot be ignored [1]. Current research efforts are directed toward phasing out the vehicles that are fuelled by fossil fuels and developing zero-emission vehicles instead [2]. Therefore, zero-emission vehicles such as battery electric vehicles (BEVs) and fuel cell electric vehicles (FCEVs), are attracting increasing attention worldwide. However, the heating demand for BEVs

in the cold season, particularly in polar and sub-polar regions, faces a huge challenge due to the lack of waste heat compared to ICEVs. Zhang *et al.* [3] concluded that the heating load varies between 3.3 kW and 6.8 kW at -20 °C in terms of vehicle speed (see Table 1).

Although the positive temperature coefficient (PTC) heater is the initial solution that can provide enough heat for cabin comfort [4], the reduction in driving range (around 50% [5]), caused during heating, results in a mileage concern for the driver [6]. The mobile air source heat pump (ASHP) which is widely used in residential space heating is seen as a good alternative to the PTC heater. It provides heat for space heating by extracting heat energy from the source with a lower

* Corresponding author.

E-mail addresses: yiji.lu@glasgow.ac.uk (Y. Lu), zhibin.yu@glasgow.ac.uk (Z. Yu).

¹ The two authors have the same contribution to this study.

| Nomenclature | |
|------------------------|--|
| Symbols | |
| A | area [cm ²] for fuel cell [m ²] for heat exchanger |
| Ac | circulation area [m ²] |
| BC | battery capacity [kWh] |
| Bo | boiling number |
| C _{O2} | oxygen concentration at the catalyst interface |
| CO | convective number |
| Cv | EEV flow coefficient |
| D _h | hydraulic diameter [m] |
| E | entropy [J/kgK] |
| F | Faraday's constant 96,485 [coulombs/mol] |
| Fr | Froude number |
| g | gravitational acceleration 9.8 [m/s ²] |
| G | mass flux [kg/m ² s] |
| Ga | Galileo number |
| h | heat transfer coefficient |
| H | enthalpy [J/kg] |
| i | current density [A/cm ²] |
| i _{fg} | enthalpy of vaporization [J/kg] |
| I | current [A] |
| Ja | Jakob number |
| k | conductivity |
| l | thickness [cm] |
| \dot{m} | Mass flow rate [kg/s] |
| M | molecular weight [kg/mol] |
| Nu | Nusselt number |
| P | partial pressure [atm] |
| Pr | Prandtl number |
| Q | heat [W] |
| q'' | Heat flux [W/m ²] |
| R | universal gas constant 8.31447 [kPa·m ³ /(kmol·K)] |
| Re | Reynolds number |
| R _{ions} | ionic resistance |
| R _{electrons} | electronic resistivity |
| R _m | membrane specific resistivity |
| T | temperature [K] |
| V | voltage [V] |
| W | energy consumption |
| X | vapor quality |
| X _{tt} | turbulent-turbulent Lockhart Martinelli parameter |
| Greek symbol | |
| γ | wetting level of membrane |
| ρ | density [kg/m ³] |
| μ | dynamic viscosity [Pa·s] |
| η ₀ | overall surface efficiency |
| η _{isen} | isentropic effectiveness |
| φ | void fraction |
| γ | compressing ratio |
| Subscripts | |
| act | activation loss |
| annular | annular flow |
| amb | ambient |
| bat | battery |
| c | cold |
| cell | single fuel cell |
| ch | battery charging |
| cl | coolant |
| comp | compressor |
| con | concentration loss |
| cond | condenser |
| dis | compressor discharging |
| dch | battery discharging |
| eva | coolant |
| ele | electrons |
| f | fin area |
| forced | forced flow |
| FC | fuel cell |
| h | hot |
| hp | heat pump |
| H ₂ | Hydrogen |
| H ₂ O | Water |
| irr | irreversible |
| IHX | internal heat exchanger |
| l | liquid |
| lo | liquid only |
| m | mean |
| nernst | nernst open circuit |
| ohm | ohmic losses |
| O ₂ | oxygen |
| OC | open circuit |
| OHX | external heat exchanger |
| ref | refrigerant |
| rev | reversible |
| sub | subcooling |
| suc | compressor suction |
| tot | total |
| v | vapor |
| wall | wall of heat exchanger |
| wavy | wavy flow |
| Acronyms | |
| AC | alternating current |
| ASHP | air source heat pump |
| BEV | battery electric vehicle |
| COP | coefficient of performance |
| DC | direct current |
| EEBC | equivalent effective battery capacity |
| EEV | electronic expansion valve |
| EV | electric vehicle |
| EVASHP | electric vehicle air source heat pump |
| FCBEV | fuel cell battery electric vehicle |
| LMTD | logarithmic mean temperature difference |
| NEDC | new European driving cycle |
| PEMFC | proton-exchange membrane fuel cell |
| PTC | positive temperature coefficient |
| SOC | state of charge |
| VI | vapour injection |

temperature [7]. However, due to the limited space in the vehicle and the COP of the essential heat pump, an ASHP system struggled to provide sufficient heat energy and the COP was marginally less than or greater than 2 in cold climates [8,9]. In order to improve the performance of the heat pump used in EVs, different approaches have been investigated and reported by scholars. For example, introducing vapour injection (VI)

technologies to the system or investigating alternative working refrigerants. Qin *et al.* [10] designed an R134a vapour injection heat pump system for EVs with single and triple portholes on a scroll compressor. The proposed system can offer a heating capacity of 3.6 kW but with a low COP of 1.7, at the ambient temperature of -20 °C. Nevertheless, when the ambient temperature increased to 0 °C, the COP increased to 2

Table 1
Value of empirical parametric coefficient of activation losses [28].

| Parameter | Value | Unit |
|------------|------------------------|------|
| α_1 | -0.944 | V |
| α_2 | 3.54×10^{-3} | V/K |
| α_3 | 80×10^{-5} | V/K |
| α_4 | -1.96×10^{-4} | V/K |

with the same heating capacity and the maximum heating capacity of approximately 4 kW was achieved. Similarly, results from other research on the VI R134a heat pump systems also showed a heating capacity between 2.5 kW and 3.5 kW and a COP range from 1.5 to 2.5 from below -20°C to -10°C [11–15]. Therefore, the improvement effect of VI systems is limited, although it can improve the heating capacity to a certain extent, the COP cannot be improved significantly. Meanwhile, some scholars discussed the application of CO_2 heat pumps for EVs. Wang *et al.* [16] investigated a CO_2 heat pump with a series gas cooler for EVs in order to utilise the heat of mid-temperature refrigerant. At -20°C , the novel CO_2 heat pump system provided at most 6.8 kW heat and the COP was 2.2 with a 10Mpa discharging pressure. Compared to the traditional CO_2 system, the suggested system improved the COP and heating capacity by 35% and 33.7% respectively. Dong *et al.* [17] provided an experimental study on CO_2 EVs' heat pumps, and concluded that the proposed system could supply up to 7.5 kW heat with a COP of 2.16 and a compressor speed of 7500RPM at a temperature of -20°C . However, different from the R134a heat pump system, the COP of the CO_2 system decreased with the increase of the ambient temperature [16,17]. Therefore, considering the heat pump in EVs as an isolated component makes it difficult to improve heating capacity and COP simultaneously.

An electric vehicle is a combination of several subsystems such as a heat pump, battery pack, and motor. Hence, effective integration of such subsystems to recover heat and use it for cabin heating has the potential to increase the performance of a heating system of EV and eventually increase its driving range. However, most of the system-level thermal management systems were from cabin and battery cooling perspectives [18–20], and only a limited number of studies considered utilising the waste heat for heating. Tian *et al.* [21] assessed a heat pump integrated thermal management system that can collect the waste heat generated by the battery, motor and controller. They assumed that those components could provide 2 kW waste heat at -5°C to 5°C and with COP ranging between 2.05 and 4.71. Jeff *et al.* [22] carried out an analysis of the whole EV thermal system including motor, transmission, thermal battery, cabin exhaust, and battery waste heat and created 32 operating modes. The outcomes indicated that dynamically selecting operating modes could lead to an average energy saving of 14.8%. However, it should be noted that, in the Warmup cycle, none of the combinations met the requirement when the ambient temperature was at -20°C . In the case of the New European Driving Cycle (NEDC) test cycle, those combinations were useless once the temperature was below 0°C . Ding *et al.* [23] developed a distributed multiple-heat source for a large electric vehicle. It used the waste heat from the battery and motor directly to heat the front and back of the vehicle. An air-source heat pump was introduced for the middle section of the vehicle. The results showed the proposed design could save 60% of energy when running for 2hours at -22°C atmospheric temperature. As well as pure EVs, the fuel cell electric vehicle is also a solution for the zero-emission vehicle. Although electric vehicles integrating with fuel cells only accounted for less than 1% of 2018's vehicle market, it is expected to play a critical role in the future of zero-emission vehicles [24]. The fuel cell is a component that can generate heat and electricity at the same time. However, most of the research about fuel cells were from the fuel cell cooling aspect [25] and less attention has been paid to recovering and using waste heat from fuel cell along with the battery for cabin heating. Lee *et al.* [26] experimentally investigated a coolant-source heat pump for fuel cell EVs by

using a triple fluid exchanger and waste heat from the fuel cell and electric device. They suggested that using a coolant-source heat pump can improve the driving range by up to 10.8% compared to using a PTC heater.

The literature indicates that thermal management of an EV based on an isolated heat pump system has been widely investigated only as an isolated heat pump system. However, the results illustrate that it is difficult to improve the heating capacity and COP simultaneously when considering the heat pump as an isolated component. Whilst there has been limited studies conducted into the heating solution from a systematic perspective, it has been shown that compensation from battery waste heat was still not sufficient for extreme cold weather although it could improve the COP in a mild-cold environment.

Therefore, in extremely cold weather, the driving range of an electric vehicle is still significantly reduced due to the need for heating, since a large proportion of the electricity generated by the battery is consumed for the heating effect. Another issue is that most research to date has ignored the frost phenomenon on the outdoor heat exchanger (OHX) that occurs after prolonged operation of the heat pump, which can cause fluctuations in cabin temperature during defrosting. Furthermore, although fuel cells can provide certain waste heat, less attention has been paid to utilising them for cabin heating. Therefore, it is necessary to further investigate how to provide sufficient heat and more importantly, to provide a relatively high COP for EVs' cabin heating at the same time under extremely cold conditions. Additionally, it is crucial to identify a way to avoid the OHX frosting. Meanwhile, management of the waste heat from the fuel cell to reduce the driving range deduction while heating the cabin also needs further investigation.

In this context, in order to provide sufficient and stable heat to the cabin with high COP, this study proposes a heating system integrating a heat pump and battery. Based on the existing heat pump system, a small fuel cell stack is introduced as a backup to the system for effective thermal management of an EV cabin and thus increase the driving range. In this system, the waste heat generated by the fuel cell stack and the battery pack are considered the source of heat for cabin heating by using a coolant heat pump. A numerical model is developed in MATLAB, which comprised three interconnected sections namely, the heat pump, fuel cell cooling subsystem and refrigerant-based battery thermal management system. The heat transfer coefficient of plate heat exchangers and fin and tube heat exchangers for R134a, battery and fuel cell heat generation model and compressor in the subsystems are investigated and validated. End of the study, the performance of the proposed system is evaluated in detail in terms of the COP, the outlet air temperature, and the heating capacity. A comparison analysis is introduced by comparing the proposed system to a conventional system in order to examine the advantages of the proposed system. The investigation into the proposed integrated system will help tackle the heating problems of current BEVs and extend the driving range in extremely cold weather. This research will be useful for expanding the operating conditions of EVs and promoting the development of EVs to create the net-zero world. This work integrates a heat pump, battery, and fuel cell together to utilise their waste heat which may not only be applied to a zero-emission vehicle but can also be of interest for domestic heat and electricity cogeneration.

2. System description

The schematic diagram of thermal management for proposed FCBEVs is shown in Fig. 1. Unlike existing systems that employ an air source heat pump to extract heat from the low-temperature ambient air with a PTC heater as a backup to cover the extreme cold weather, the proposed system in this study introduces a coolant source heat pump and a fuel cell system to replace the PTC heater in order to utilise waste heat and provide high-efficiency heat and electricity cogeneration for the vehicle. In the proposed system, waste heat from the fuel cell stack and the battery pack was utilised as a supplement for space heating. The green line, in Fig. 1, represents the R134a refrigerant flow cycle. After

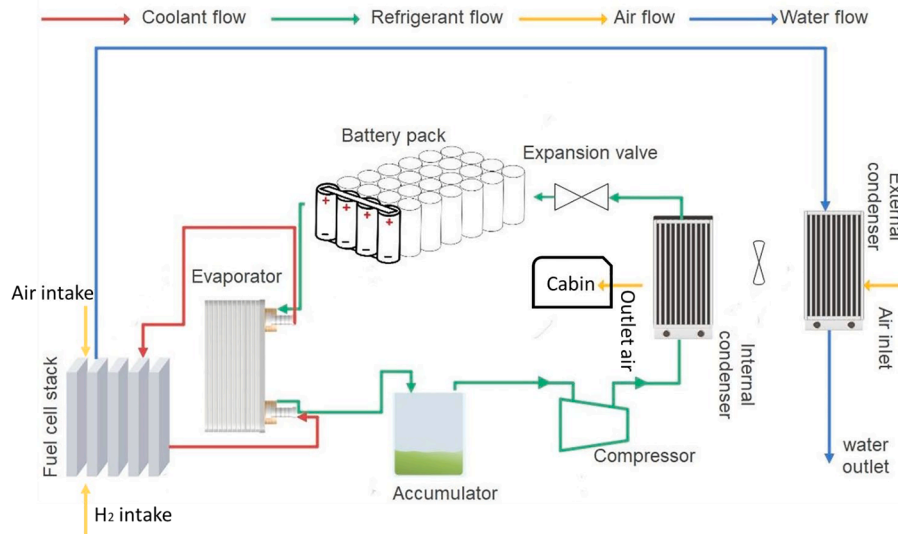


Fig. 1. Schematic diagram of the heat pump assisted thermal management system for fuel cell backup battery-powered electric vehicles.

the expansion valve, the refrigerant first passes by the battery pack. The battery thermal management system is designed as a refrigerant-based cooling system. The refrigerant flows through the battery pack to absorb the waste heat generated during the battery charging and discharging process. The refrigerant then enters a counter-flow plate-type evaporator where heat is absorbed from the coolant (red line) coming from the fuel cell stack and converted into complete vapour. The coolant comes out of the plate heat exchanger and then goes back to the fuel cell stack to cool down the fuel cell continuously. The function of the accumulator is to separate gas and liquid refrigerant to make sure only vapour-phase refrigerant can access the compressor. After the processing of the compressor, pressure, and temperature both increases. The high-pressure and high-temperature refrigerant runs into the fin-tube type crossflow internal condenser. In the condenser, the refrigerant undergoes a heat transfer procedure with the feeding air which will be supplied to the cabin to achieve thermal comfort. The refrigerant from the internal condenser flows past the expansion valve and the cycle continues. The cabin supply air sourced from the environment first flows across the external fin and tube-type heat exchanger for pre-heating by recovering heat from the hot water produced during the fuel cell reaction represented by the blue line. Operating parameters should be adjusted, such as lowering the fuel cell current output to avoid the freezing point of the water inside the external heat exchanger due to the heat transfer with the cold ambient air. Subsequently, the pre-processed cabin supply air passes over the internal heat exchanger before entering the cabin.

The air intake for the fuel cell comes from the ambient environment

and is compressed to high pressure and high temperature by an air compressor (not shown in the diagram) before flowing into the fuel cell stack. H₂ for the fuel cell comes from the onboard hydrogen vessel.

The electricity flow operating in the proposed FCBEV with a heat pump is shown in Fig. 2. A fuel cell stack of required capacity is installed in the areas where pure BEV battery packs have been installed, which generates current during the proton exchange procedure between H₂ and air cross proton-exchange membranes. The fuel cell output current is passed through a DC/DC converter to amplify its voltage to the battery pack level. The Li-ion battery pack still works as the main engine that supplies power to the motor, compressor and other electrical components that are not included in Fig. 2 such as pumps and fans through a DC/AC inverter. However, unlike the common BEVs, the battery pack can be simultaneously recharged on-board by the current generated by the fuel cell in the proposed FCBEV.

3. Model development

3.1. PEM fuel cell heat generation model

The heat generated by the fuel cell is a by-product produced while it is generating power, hence the heat generation model of a Proton-exchange membrane fuel cell (PEMFC) can be introduced by using electro-chemical and thermodynamic theories. The amount of heat generated from a single fuel cell is defined by current and voltage as Eq. (1):

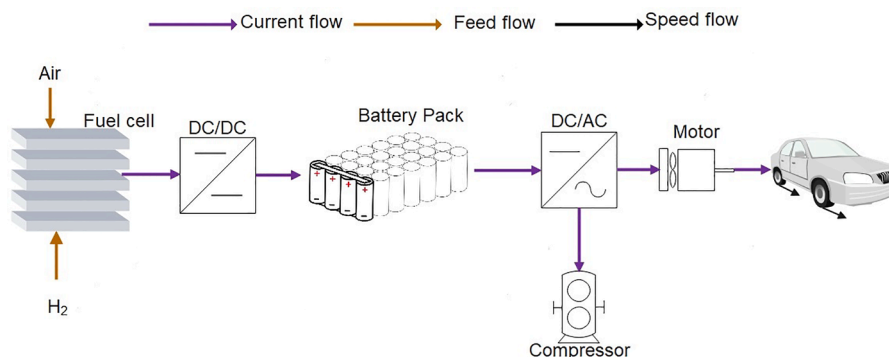


Fig. 2. Schematic diagram of fuel cell backup battery-powered electric vehicles.

$$Q_{FC} = (V_{nernst} - V_{cell}) \times I_{FC} \quad (1)$$

where V_{nernst} is the Nernst open-circuit voltage, V_{cell} is the voltage of the single-cell and I_{FC} is the current generated by the single fuel cell. The equation of Nernst open circuit voltage is expressed as Eq. (2), where P_{H_2} is hydrogen partial pressure, P_{O_2} is oxygen partial pressure and T_{FC} is the temperature of the fuel cell [27].

$$V_{nernst} = 1.228 - [0.85 \times 10^{-3} \times (T_{FC} - 298.15) - 4.3086 \times 10^{-5} \times T_{FC} \times \ln(P_{H_2} \times P_{O_2}^{0.5})] \quad (2)$$

The voltage of a single fuel cell V_{cell} can be presented as shown by Eq. (3).

$$V_{cell} = V_{nernst} + V_{act} + V_{ohm} + V_{con} \quad (3)$$

where V_{act} , V_{ohm} and V_{con} are activation losses, ohmic losses and concentration, respectively. The term V_{act} is presented as a function of oxygen concentration at the catalyst interface C_{O_2} , I_{FC} and T_{FC} as given by Eq. (4), Mann et al. [28].

$$V_{act} = \alpha_1 + \alpha_2 \times T_{FC} + \alpha_3 \times T_{FC} \times \ln(C_{O_2}) + \alpha_4 \times T_{FC} \times \ln(I_{FC}) \quad (4)$$

The value of C_{O_2} can be obtained from an expression of Henry's law [29].

The V_{ohm} is defined as shown by Eq. (5).

$$V_{ohm} = -I \times (R_{ions} + R_{ele}) \quad (5)$$

where R_{ele} is the electronic resistivity which can be ignored [30] while R_{ions} as the ionic resistance is a function of membrane specific resistivity R_m , membrane thickness l_{FC} and membrane surface area A_{FC} , as given by Eq. (6) [31].

$$R_{ions} = \frac{R_m \times l_{FC}}{A_{FC}} \quad (6)$$

In which:

$$R_m = \frac{181.6 \times [1 + 0.03 \times (\frac{l_{FC}}{A_{FC}}) + 0.062 \times (\frac{T_{FC}}{303})^2 \times (\frac{l_{FC}}{A_{FC}})^{2.5}]}{[\gamma - 0.634 - 3 \times (\frac{l_{FC}}{A_{FC}})] \times e^{[4.18 \times (\frac{T_{FC}-303}{T_{FC}})]}} \quad (7)$$

The value of γ is determined by the wetting level of the membrane, and is 0, 14, and 23 for dry, saturated and oversaturated membranes [31].

The final term on the right-hand side of Eq. (3) V_{con} is calculated as given by Eq. (8) [32].

$$V_{con} = \frac{3 \times R \times T_{FC}}{4 \times F} \times \ln(1 - \frac{i_{FC}}{i_{FC_{max}}}) \quad (8)$$

where R is the universal gas constant and F is Faraday's constant, i_{FC} is the current density of the fuel cell and $i_{FC_{max}}$ is the maximum current density which is assumed to be equal to 2.2 A/cm² [33].

$$i_{FC} = \frac{I_{FC}}{A_{FC}} \quad (9)$$

The consumption of hydrogen and water generation during fuel cell stack reaction are given in Eq. (10) and Eq. (11) [34].

$$\dot{m}_{H_2} = \frac{I_{FC} \times M_{H_2} \times N_{FC}}{2 \times F} \quad (10)$$

$$\dot{m}_{H_2O} = \dot{m}_{H_2} \times \frac{M_{H_2O}}{M_{H_2}} \quad (11)$$

where M_{H_2} and M_{H_2O} are the molecular weight of H₂ and H₂O. Air and H₂ utilization in this model are assumed to be 100%.

The operational and geometrical details of the fuel cell are provided in Table 2. The model of the fuel cell heat generation is verified with the experimental results of Liso et al. [33] and exhibits a deviation of 5%, as

Table 2
Parameters for fuel cell model and battery [37].

| Specification | Value | Unit |
|--|----------------------|-----------------|
| Fuel cell | | |
| Fuel cell Operating temperature T_{FC} | 65 | °C |
| Inlet O ₂ pressure P_{O_2} | 2.5 | atm |
| Inlet H ₂ pressure P_{H_2} | 2.4 | atm |
| Current output I_{FC} | 190–230 | A |
| Number of cells N_{FC} | 40 | / |
| Area of cell A_{FC} | 285.8 | cm ² |
| Thickness of cell l_{FC} | 5.1X10 ⁻³ | cm |
| Battery | | |
| Battery capacity | 8 | Ah |
| Battery voltage | 4.2 | V |
| Number of batteries | 1764 | / |
| Number of batteries in series for one module | 6 | / |
| Number of batteries in parallel for one module | 21 | / |
| Number of modules | 14 | / |
| SOC | 0.5 | / |
| Battery operating temperature | 30 | °C |
| Voltage of battery pack | 352 | V |
| Battery pack capacity | 60 | kWh |

shown in Fig. 3.

3.2. Battery thermal model

The heat generation of a battery cell can be divided into two parts, which are irreversible heat Q_{irr} and reversible heat Q_{rev} [35]:

$$Q_{battery} = \underbrace{I_{ch/dch}^2 \times R_{ch/dch}}_{irr} - \underbrace{I_{ch} \times T_{bat} \times \frac{dE_{OC_{bat}}}{dT_{bat}}}_{rev} \quad (12)$$

where $R_{ch/dch}$ is the internal thermal resistance of a single battery while charging or discharging. $\frac{dE_{OC_{bat}}}{dT_{bat}}$, is called the entropy coefficient. The experimental data of both of these two parameters under different State of Charge (SOC), temperature, and the specifications for battery are obtained from ref. [36]. The battery pack was designed based on the Tesla Model S released in 2013 with a 60-kWh pack. The details are presented in Table 2 [37].

The thermal model of the battery is validated by examining the heat generation while discharging and the internal resistance is calculated while charging and is compared with Liu et al. [36], as shown in Fig. 4(a) and (b) respectively. The predicted heat generation deviates by ±10%

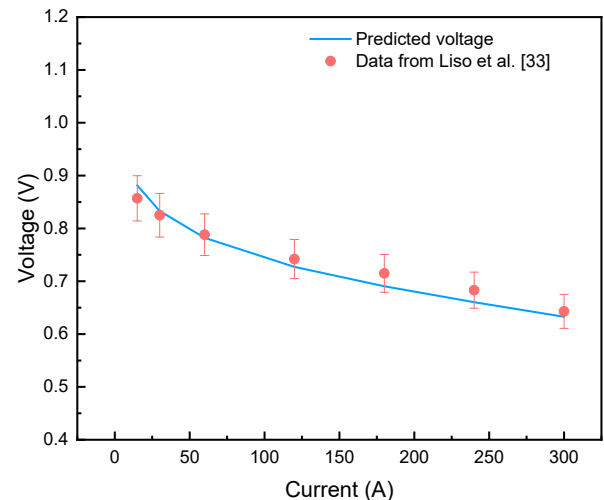


Fig. 3. Validation of fuel cell heat generation model.

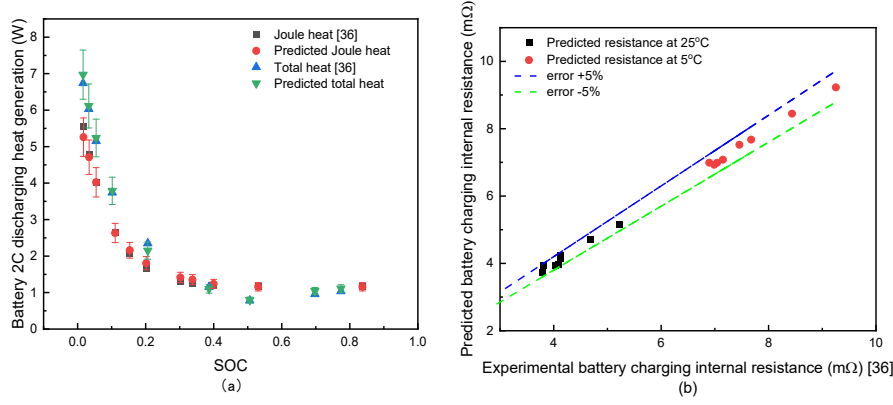


Fig. 4. Validation results of the battery thermal model under discharging (a) and charging (b) scenarios.

compared to Liu *et al.* [36] and predicted internal resistance is well within the error band of $\pm 5\%$.

3.3. Heat transfer model of heat exchanger

The evaporator adopts a counter-flow plate heat exchanger. The refrigerant flows from one side while the coolant flows from the other side. Whereas, the internal air-cooled fin and tube type of heat exchanger is considered as a condenser and the external ones for waste heat recovering from H_2O is seen as the evaporator. The geometrical information of the three heat exchangers considered in the proposed FCBEV is presented in Table 3.

The same amount of heat absorbed or released by the primary refrigerant in the heat exchangers is exchanged with the secondary fluid, as the heat loss between the heat exchanger and the atmosphere is negligible. Hence, the heat balance across heat exchangers is expressed as shown in Eq. (13) to (15).

$$Q_{eva/cond/OHX} = \dot{m}_{cl/air/H_2O} \times Cp_{cl/air/H_2O} \times \Delta T_{cl/air/H_2O} \quad (13)$$

$$Q_{ref} = \dot{m}_{ref} \times (1 - X_{inlet}) \times i_{fg} \quad (14)$$

$$Q_{eva/cond/OHX} = U_{eva/cond/OHX} \times A_{eva/cond/OHX} \times LMTD_{eva/cond/OHX} \quad (15)$$

where the logarithmic mean temperature difference (LMTD) is described as:

$$LMTD = \frac{\Delta T_1 - \Delta T_2}{\ln(\Delta T_1/\Delta T_2)} \quad (16)$$

with

Table 3

The specification of heat pump components.

| components | Specification | Value | Unit |
|-----------------------|------------------|----------------------|-----------------|
| Fuel cell evaporator | type | Plate heat exchanger | / |
| | Number of plates | 110 | / |
| | Plate size | 120 × 330 | mm ² |
| | Channel space | 2.9 | mm |
| Internal condenser | type | Fin-Tube | / |
| | inner diameter | 7 | mm |
| | Internal area | 2.086 | m ² |
| | External area | 8.344 | m ² |
| Air preheat condenser | type | Fin-Tube | / |
| | Inner diameter | 8.2 | mm |
| | Internal area | 0.2865 | m ² |
| | External area | 0.3725 | m ² |
| Inverter Compressor | type | Scroll | / |
| | Displacement | 27 | cc/rev |
| | Compressor speed | 3000–5000 | rpm |

$$\Delta T_1 = T_{h,inlet} - \Delta T_{c,outlet} \quad (16a)$$

$$\Delta T_2 = T_{h,outlet} - \Delta T_{c,inlet} \quad (16b)$$

It should be noted that for cross-flow a correction factor should be imposed to Eq. (16) and the value of the correction factor can be obtained from ref. [38].

The overall heat transfer coefficient for a plate heat exchanger, i.e. evaporator, can be calculated as below:

$$\frac{1}{U_{eva}} = \frac{1}{h_{cl}} + \frac{1}{h_{eva,ref}} + \frac{\delta_{wall}}{\lambda_{wall}} \quad (17)$$

where δ_{wall} and λ_{wall} are thickness and thermal conductivity of the plate, respectively. The two-phase heat transfer coefficient correlation for the refrigerant side is expressed as [39]:

$$h_{eva-ref} = 1.055 \times [1.056 \times Co^{-0.4} + 1.02 \times Bo^{0.9}] \times X_m \times h_{lo} \quad (18)$$

where Co is the convective number and Bo is the boiling number, defined as.

$$Co = \frac{(\rho_v)^{0.5}}{\rho_l} \times ((1 - X_m)/X_m)^{0.8} \quad (19)$$

$$Bo = \frac{\dot{q}_{wall}}{G_{ref-eva} \times i_{fg}} \quad (20)$$

in which ρ_v and ρ_l are the density of vapour and liquid refrigerant, X_m is the mean vapour quality in the evaporator. \dot{q}_{wall} is the heat flux through the wall, $G_{ref-eva}$ is the mass flux of refrigerant in a plate-type evaporator while i_{fg} is the enthalpy of vaporization.

Single-phase heat transfer coefficient correlation h_{lo} was modified by [39] based on [40]:

$$h_{lo} = 0.2875 \times Re^{0.78} \times Pr^{1/3} \times \frac{k_l}{D_h} \quad (21)$$

where D_h is hydraulic diameter, k_l is the conductivity of liquid refrigerant, Re is the Reynolds number and Pr is the Prandtl number.

For the coolant side, the single-phase heat transfer coefficient was conducted as [40]:

$$h_{cl} = 0.2121 \times Re_{cl}^{0.78} \times Pr^{1/3} \times \left(\frac{\mu_m}{\mu_{wall}}\right)^{0.14} \times \left(\frac{k_{cl}}{D_{h-eva}}\right) \quad (22)$$

in which μ_m and μ_{wall} are calculated based on the average bulk fluid and wall temperature in the evaporator. For fin and tube heat exchanger i.e. condenser, the overall heat transfer coefficient is shown as:

$$\frac{1}{U_{cond}A_{cond}} = \frac{1}{\eta_0 \times h_{air_cond} \times A_c} + R_{wall} + \frac{1}{\eta_0 \times h_{ref_cond} \times A_h} \quad (23)$$

where A_c and A_h are the surface areas of the cold side and hot side respectively and η_0 is the overall surface efficiency which equals to:

$$\eta_0 = 1 - \frac{A_f}{A_{tot}} \times (1 - \eta_f) \quad (24)$$

in which A_f and A_{tot} stand for total fin area and total area respectively and η_f is the efficiency of a single fin which can be located in [38].

Two different heat transfer principles for the refrigerant side are calculated below [41]. For wavy flow:

$$Nu_{wavy} = \frac{0.23 \times Re_{v_ref}^{0.12}}{1 + 1.11 \times X_{II}^{0.58}} \times \left[\frac{Ga \times Pr_{I_1}^{0.25}}{Ja_I} \right] + \cos^{-1}(2 \times \varphi - 1) / \pi \times Nu_{forced} \quad (25)$$

$$Nu_{forced} = 0.0195 \times Re_I^{0.8} \times Pr_I^{0.4} \times \sqrt{1.376 + c_1 / X_{II}^{c_2}} \quad (26)$$

When $0 < Fr_I \leq 0.7$, Eq. (27a) and (27b) apply:

$$c_1 = 4.172 + 5.48 \times Fr_I - 1.564 \times Fr_I^2 \quad (27a)$$

$$c_2 = 1.773 - 0.169 \times Fr_I \quad (27b)$$

When $Fr_I > 0.7$ Eq. (28a), (28b) apply:

$$c_1 = 7.242 \quad (28a)$$

$$c_2 = 1.655 \quad (28b)$$

while for annular flow:

$$Nu_{annular} = 0.023 \times Re_I^{0.8} \times Pr_I^{0.4} \times \left[1 + \frac{2.22}{X_{II}^{0.89}} \right] \quad (29)$$

In Eqs. (22) to (29), X_{II} is the turbulent-turbulent Lockhart Martinelli parameter, Ga is the Galileo number, Fr_I is the Froude number, Ja_I is the liquid Jakob number, φ is the void fraction. Expressions of those parameters are shown below:

$$X_{II} = \left(\frac{\rho_v}{\rho_l} \right)^{0.5} \times \left(\frac{\mu_l}{\mu_v} \right)^{0.1} \times \left(\frac{1 - X_m}{X_m} \right)^{0.9} \quad (30)$$

where μ is dynamic viscosity.

$$Ga = g \times \rho_l \times (\rho_l - \rho_v) \times \frac{D_h^3}{\mu_l^2} \quad (31)$$

$$Fr_I = \frac{G_{ref_cond}^2}{\rho_l^2 \times g \times D_h} \quad (32)$$

$$Ja_I = C_{p_ref_l} \times (T_{cond} - T_{wall}) / i_{fg} \quad (33)$$

in which $C_{p_ref_l}$ is the specific heat at constant pressure for liquid refrigerant, T_{cond} and T_{wall} is the condensing temperature and wall temperature respectively. The void fraction was described as [42]:

$$\varphi = \left[1 + \frac{1 - X_m}{X_m} \times \left(\frac{\rho_v}{\rho_l} \right)^{\frac{2}{3}} \right]^{-1} \quad (34)$$

Heat transfer coefficients on the refrigerant side of the condenser can be calculated from Nu :

$$Nu_{wavy/annular} = \frac{h_{cond_ref} \times D_h}{k_{l_ref}} \quad (35)$$

For the air side, a simple heat transfer model was adopted as introduced in ref [38]:

$$h_{air_cond} = C \times Re_{air}^m \times Pr^{1/3} \quad (36)$$

where the constants C and m are listed in Table 4.

The verification of the evaporator and condenser are illustrated in Fig. 5. (a) and (b) according to the experimental outcomes achieved by ref. [40] and ref. [41], respectively. For both heat exchangers, all predicted values fall with an error band of $\pm 10\%$.

3.4. Compressor model and electronic expansion valve (EEV)

The compressor with variable speed is adopted in the current analysis and the quadratic relation between pressure ratio γ and refrigerant mass flow rate is developed using data from ref. [43]. The correlation is shown in Eq. (37). The results were validated by ref. [44] as shown in Fig. 6. and the specification of the compressor is shown in Table 3.

$$\gamma = -1566 \times \dot{m}_{ref}^2 + 218.83 \times \dot{m}_{ref} - 3.4801 \quad (37)$$

The mass flow rate through the EEV is calculated from ref. [21].

$$\dot{m}_{EEV} = C_v A_c \sqrt{2 \times \Delta P_{EEV} \times \rho_{ref_in}} \quad (38)$$

where C_v is the flow coefficient, $C_v = 0.02005 \times \sqrt{\rho_{in}} + 0.634 / \rho_{out}$; A_c is the circulation area.

3.5. Simulation procedure

Each model described above is coupled to form the proposed thermal management system based on the following assumption.

- (1) Coolant temperature at the outlet of the fuel cell stack was fixed i. e. 30 °C.
- (2) The pressure drop across heat exchangers and inside pipe and heat loss between the heat exchanger and surroundings are neglected.
- (3) Fuel cell stack's heat loss was ignored, but the heat loss of the battery pack was calculated under a constant airspeed of 0.5 m/s, according to the investigated battery discharging rate.
- (4) The power consumption of the fan and pump were omitted and the inlet air flow rate would not be affected by the vehicle speed.
- (5) The difference between the minimum temperature of the coolant in the evaporator and R134a evaporating temperature is assumed as constant i.e. 2 °C.
- (6) The refrigerant at the evaporator outlet is assumed as the saturated vapour and an accumulator was installed before the compressor to make sure only gas can enter the compressor.

The thermal management simulation model of the proposed FCB-EV has been organised as presented in Fig. 7. The model is developed in MATLAB and the thermal properties are obtained by coupling REFPROP with MATLAB code. The simulation started from the PEMFC thermal management side in order to dissipate all the heat generated from PEMFC and to be utilised by the cabin heating system. The cooling capacity of the cold end of the heat pump will be adjusted based on the fuel cell power output and battery discharging C rate. So, with the increasing or decreasing waste heat generation, our system's capacity will also be changed to make sure the thermal equilibrium of the fuel cell stack and battery pack to avoid overcooling or temperature increase in them. Independent variables were selected based on actual application scenarios

Table 4

Constant of C and m in Eq. (36) for cross flow.

| Re _{air} | C | m |
|-------------------|-------|-------|
| 0.4–4 | 0.989 | 0.330 |
| 4–40 | 0.911 | 0.385 |
| 40–4000 | 0.683 | 0.466 |
| 4000–40000 | 0.193 | 0.618 |
| 40000–400000 | 0.027 | 0.805 |

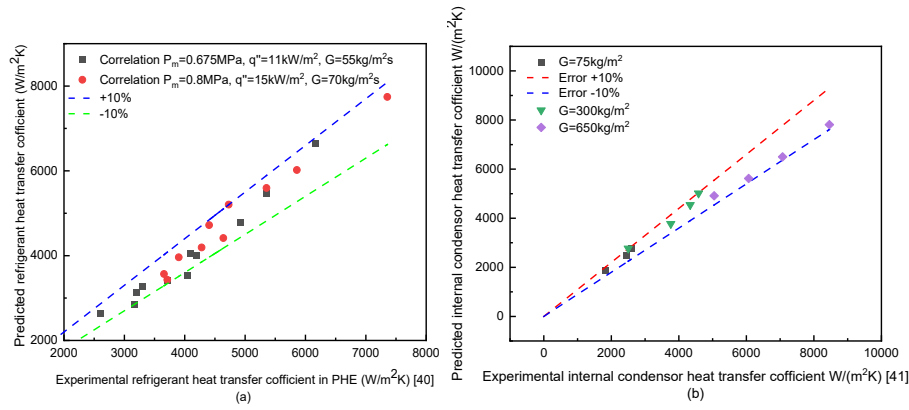


Fig. 5. Validation results of the heat exchanger heat transfer coefficient model.

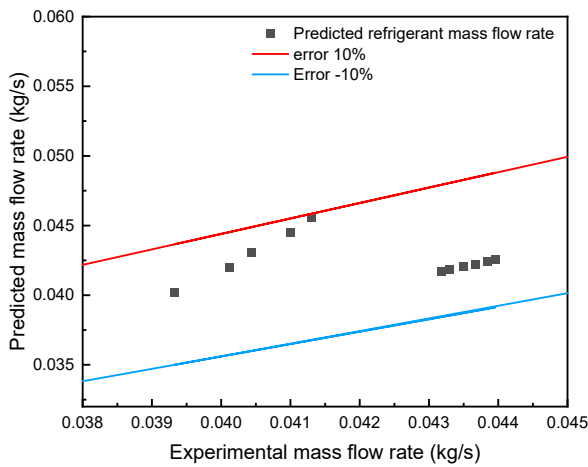


Fig. 6. Validation results of the simplified compressor model [44].

(including ambient temperature, PEMFC current output, battery discharging rate, subcooling degree, and coolant inlet temperature of the evaporator), and their operating range in the simulation are listed in

Table 5. Other parameters, including coolant mass flow rate, refrigerant mass flow rate, evaporating and condensing temperature etc. were intermediate dependent variables after the size of the evaporator, condenser and compressor were set. Those intermediate dependent variables would change to independent variables and the value of those intermediate dependent variables would be finalized by 6 iterative loops nested within each other. Fuel cell cold startup scenarios are not considered in this research. But there are some potential solutions to tackle it. For example, the quick and safe cold startup for the fuel cell stack can be achieved at $-15\text{ }^{\circ}\text{C}$ by electrochemical self-heated method

Table 5
Operating conditions in the simulation.

| Parameter | Value | Unit |
|--|------------------|--------------------|
| Ambient temperature (T_{amb}) | -25 to 5 | $^{\circ}\text{C}$ |
| Coolant inlet temperature at the entrance of evaporator ($T_{cl,eva,inlet}$) | 27 to 33 | $^{\circ}\text{C}$ |
| Fuel cell current output (I_{FC}) | 190 to 230 | A |
| Battery discharging rate (C_{dch}) | 0.19 to 0.26 | C |
| Subcooling degree (T_{sub}) | 0 to 4 | $^{\circ}\text{C}$ |
| Refrigerant | R134a | / |
| Coolant | Egl-5050 | / |

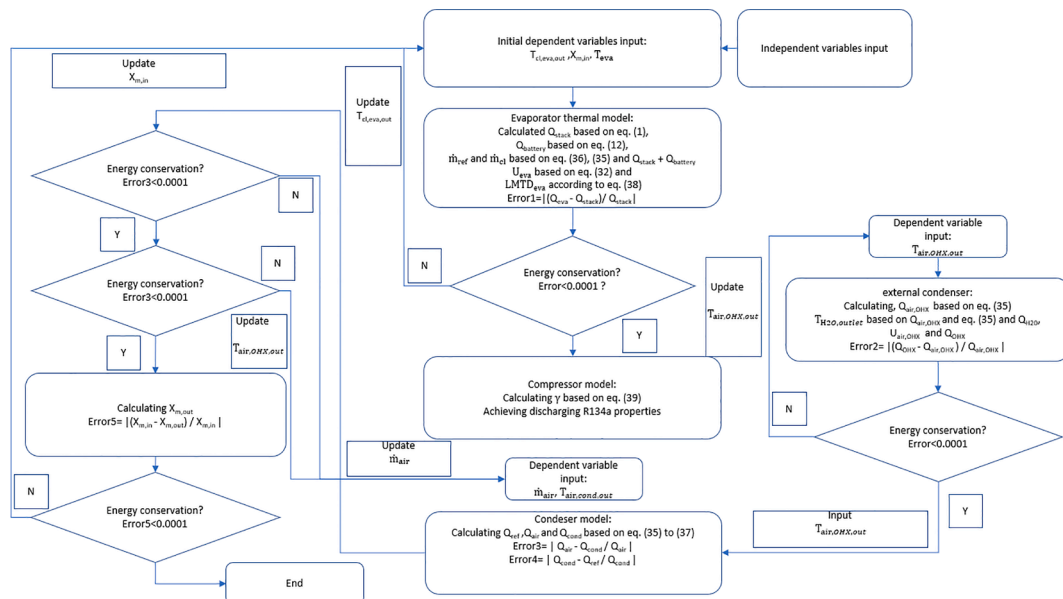


Fig 7. Flow chart of proposed system simulation.

[45] or using a heat pump and PTC heater [46] powered by battery as supplements when facing more severe conditions.

The proposed model was assumed to be converged when energy balances across heat exchangers as represented by Eq. (13) to (15) were achieved.

3.6. Performance indicators

COP is a critical performance for heat pump-based heating systems, as it will be affected by any of the parameters inside the system. The COP of a heat pump system is calculated as Eq. (39).

$$COP = \frac{Q_{heat}}{W_{tot}} \quad (39)$$

in which Q_{heat} is the effective heat that can be input to the target area which equals to Q_{cond} while W_{tot} is the total power consumption that equals the compressor power consumption W_{comp} in this case. The expression of W_{comp} is shown as below:

$$W_{comp} = \frac{(H_{dis} - H_{suc})}{\eta_{isen}} \quad (40)$$

where H_{dis} and H_{suc} are the enthalpy of R134a at suction and discharging point respectively, η_{isen} is the isentropic effectiveness of the compressor which is assumed to be 0.67 [43].

Equivalent effective battery capacity (EEBC) is a newly defined performance index which is used to evaluate how much equivalent battery capacity can be used for driving usage in one charging cycle. The expression of EEBC is shown in Eq. (41).

$$EEBC = BC - W_{hp} + FC_{ch} \quad (41)$$

where BC , W_{hp} and FC_{ch} are the initial battery pack capacity, power consumption of the heat pump system, and supplemental battery capacity by fuel cell charging respectively.

4. Results and discussion

This section presents the influence of several operating variables such as ambient temperature, PEMFC current output, battery discharging rate, subcooling degree and coolant inlet temperature of evaporator and working fluid on the performance of the proposed FCBEV. The input ranges of the variables are presented in Table 5.

4.1. Effect of fuel cell output current

Fuel cell output current is a crucial parameter that decides the on-board battery charging speed. Fig. 8(a) illustrates the impacts of the fuel cell current output on outlet air temperature and COP. It shows that the cabin air inlet temperature inversely correlated with changes in fuel cell output current while the COP increased with the increase of fuel cell output current. The reason for this change can be explained in detail using Fig. 8(b) and (c). When the fuel cell current output increased, the waste heat from the fuel cell stack increased and vice versa as shown in Fig. 8(b). According to assumption (5), LMTD was a single-valued function of evaporator coolant outlet temperature according to Eq. (16) to (16b). The higher the LMTD the lower the evaporator coolant outlet temperature would be. In order to dissipate all the heat generated inside the fuel cell stack and keep its temperature stable, the evaporator coolant outlet temperature decreased relatively to match the increasing fuel cell current output based on Eq. (15). However, because of the difference in growth rate between ΔT_{cl} in Eq. (13) and $LMTD_{eva}$ in Eq. (15), the coolant mass flow rate descended to compensate it in order to achieve energy conservation as shown in Fig. 8(c). Although the evaporating temperature decreased in terms of the evaporator coolant outlet temperature, Fig. 8(c) demonstrates the refrigerant mass flow rate

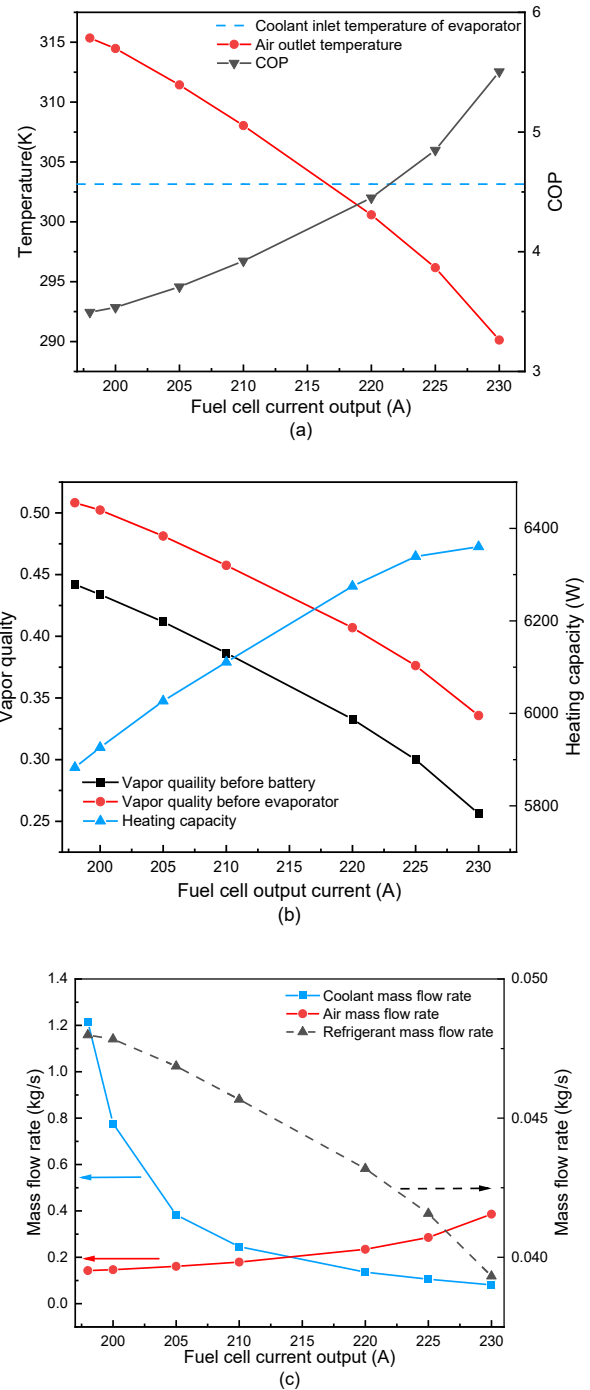


Fig. 8. (a) Variation of air temperature and COP (b) variation of vapour quality and heating capacity (c) variation of coolant, air, and refrigerant mass flow rate with respect to fuel cell output current ($T_{amb} = 0\text{ }^{\circ}\text{C}$, $T_{cl_eva_inlet} = 30\text{ }^{\circ}\text{C}$, $C_{dch} = 0.237$, $T_{sub} = 0\text{ }^{\circ}\text{C}$).

changed significantly from 0.048 kg/s to 0.039 kg/s for the given range of fuel cell output current. However, it was not sufficient for the increased cooling load of the FC stack. As a result, the vapour quality before the evaporator decreased by over 50% to increase the latent heat that was needed during evaporation as shown in Fig. 8(b). The average vapour quality in the evaporator dominates over the refrigerant flow rate during the evaporating procedure, resulting in a reduction in vapour quality [40]. Since more heat would be released through the internal condenser, increasing the air mass flow rate was the only way to raise the condenser's overall heat transfer coefficient when the inlet air

temperature could not be significantly changed. Hence, the air temperature decreased for the sake of increasing the air mass flow rate. Furthermore, with the decrease in the mass flow rate of refrigerant, the compressing ratio should decrease correspondingly and cause an increase in COP. Meanwhile, it should be noted that when the fuel cell output current exceeded a specific value, 217 A in Fig. 8(a), the outlet air temperature would be lower than the coolant temperature out of the fuel cell stack. This means if the fuel cell output current exceeded a specific point, the outlet air temperature of the proposed system may not provide a higher outlet air temperature than using coolant heating the cabin directly. Therefore, fuel cell current has an important impact on heating capacity, outlet air temperature, and COP. In order to provide not only enough heating capacity but also to supply air at a high temperature, the fuel cell current output must be well controlled when other parameters stay constant.

4.2. The impact of battery discharging rate and subcooling degree

Fig. 9 presents the impact of battery discharging rate on outlet air temperature, outlet vapour quality and COP while other independent parameters were kept constant. As shown in Fig. 9(a), the vapour quality for the battery and evaporator both decreased with the increase in battery discharging rate because of the rise of the battery's cooling demand. Notably, the vapour quality difference between battery inlet and evaporator inlet increased. The main reason for this was the proportion of heat generated by the battery increased. With the increasing waste

heat from the battery, more liquid refrigerant should transfer into vapour status. Similar to the fuel cell current output, battery discharging C rate also had a negative impact on outlet air temperature due to the increased air flow rate. Fig. 9(b) illustrates an opposite relationship between heating capacity and battery discharging C rate compared to heating capacity and fuel cell current output. With the battery discharging rate varying from 0.195 to 0.26, the system's heating capacity slightly decreased from 6.37 kW to 6.14 kW. One of the main reasons is a reduction in work undertaken by the compressor. Although the system can absorb more waste heat from the battery pack, the decreasing refrigerant mass flow rate due to the descending inlet vapour quality led to a lower compression work and the decrease is greater than the increase in waste from the battery pack. In contrast, as shown in Fig. 9(b), the COP increased with the increase of the battery discharging rate. The large increase in COP was mainly caused by the limitation of the subcooling degree. From Fig. 10, it can be seen that when there was no limitation of the subcooling degree, the cycle could run as shown in the yellow. With a small decrease in the subcooling degree, the system achieved the target with little change. However, when the subcooling degree was set as unchangeable at 0 °C, both the compressing ratio and evaporating temperature declined and led to a significant increase in COP. Hence, when the vehicle is accelerating, it would be better to increase the fuel cell output within the allowable operating range in order to compensate for the negative impact on heating capacity caused by the increasing battery discharging rate.

Fig. 11 describes the influence of the condenser subcooling degree when other independent variables are kept constant. It can be seen in Fig. 11(a), the outlet air temperature increased with an increase in the subcooling degree, but the trend of COP was the opposite. When the subcooling degree increased from 0 K to 4 K the condensing temperature increased by 10.3% correspondingly in order to increase the vapour quality after the adiabatic process of the throttle valve. For the sake of satisfying the cooling demand of the fuel cell and battery pack, the refrigerant mass flow rate increased as well due to the increase in vapour quality. Because of the constant current output from the fuel and ambient temperature, the inlet air temperature of the condenser did not change to some certain value, which meant the last term $LMTD_{cond}$ in Eq. (14) on the right-hand side increased as the condensing temperature was the only variable in this equation. In addition, because of the rising refrigerant mass flow rate, the heat transfer coefficient on the refrigerant side also increased. Reducing the air mass flow rate was the only way to control the U_{cond} in Eq. (14) to maintain the condenser's conservation of energy. Furthermore, the total amount of heat transferred through the condenser increased as a result of the introduced subcooling. Hence, the air temperature was raised as the degree of subcooling increased according to Eq. (13). However, although a certain degree of subcooling could slightly increase the heat release, the power consumption of the

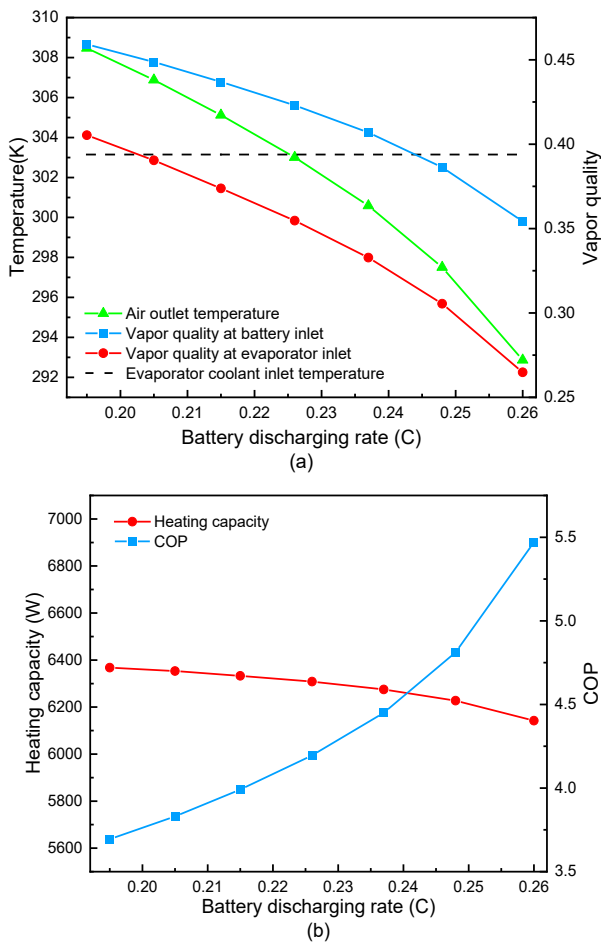


Fig. 9. The impact of battery discharging rate on (a) air outlet temperature and vapor quality and (b) heating capacity and COP ($T_{amb} = 0\text{ }^{\circ}\text{C}$, $T_{cl_eva_inlet} = 30\text{ }^{\circ}\text{C}$, $I_{FC} = 220\text{ A}$, $T_{sub} = 0\text{ }^{\circ}\text{C}$).

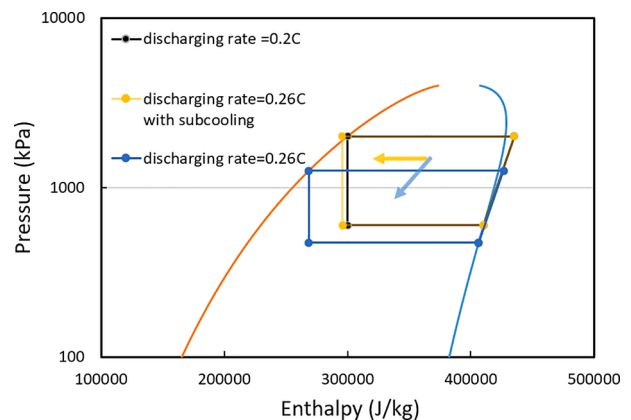


Fig. 10. Pressure to enthalpy cycle diagram under different battery discharging rate ($T_{amb} = 0\text{ }^{\circ}\text{C}$, $T_{cl_eva_inlet} = 30\text{ }^{\circ}\text{C}$, $I_{FC} = 220\text{ A}$, $T_{sub} = 0\text{ }^{\circ}\text{C}$).

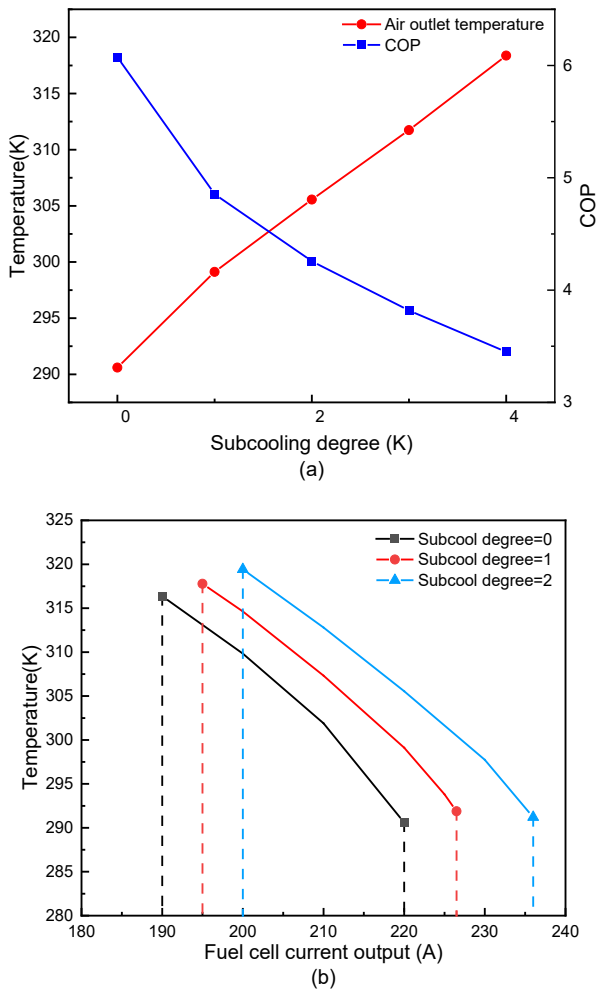


Fig. 11. The impacts of the subcooling degree on outlet air temperature and COP (a) and operating range (b) ($T_{amb} = 0\text{ }^{\circ}\text{C}$, $T_{cl_eva_inlet} = 32\text{ }^{\circ}\text{C}$, $I_{FC} = 220\text{A}$ for (a), $C_{dch} = 0.237$).

compressor due to the increase of refrigerant mass flow rate was much higher than that part of heat. The increase in compressing power dominated the change in COP and caused a 43% decrease in COP. The application of subcooling could be decided depending on the operating scenario. For example, if the passenger gets into the vehicle, body heating, such as hands and feet is more likely to have priority. In this case, adjusting the subcooling degree can help passengers feel comfortable quickly. Moreover, Fig. 11(b) displays the operating range when varying the subcooling degree. When the subcooling degree varied from 0 to 2, the operating range raised from 190A to 220A to 200A-237A. This is because when the fuel cell current output increases, the evaporation temperature of the proposed system decreases to achieve a larger temperature difference inside the evaporator, but a certain degree of subcooling can reduce the refrigerant temperature at the condenser outlet to reduce an evaporation decrease in temperature. It can be concluded that the higher the fuel cell and battery pack cooling demands, the higher the subcooling degree needed. Additionally, a higher subcooling degree can also offer increased flexibility to the system.

4.3. Effect of ambient temperature and coolant inlet temperature

Ambient air temperature used to be a very crucial parameter for BEV's air-source heat pumps. Qin et al. [47] experimentally investigated the performance of an air source R134a heat pump for EV at $-20\text{ }^{\circ}\text{C}$. As shown in Fig. 12, the heating capacity and the COP of Qin's vapour

injection heat pump system varied by 31% and 52% respectively with respect to the change in ambient temperature. However, the proposed heat pump system in this study showed a stable advantage compared to the traditional air source heat pump in BEV discussed in ref [47]. When the ambient temperature decreased, the heating capacity did not change significantly because the heat source in our study was the waste heat generated from the fuel cell stack and battery pack which was not sensitive to the ambient temperature. Meanwhile, based on the assumption (3), that the fuel cell heat dissipated to the external environment was not considered, only the battery pack's heat loss was calculated. Furthermore, although the COP of the proposed system decreased with the drop in ambient temperature, the variation was only between 4.48 and 4.31 when the ambient air temperature changed from $5\text{ }^{\circ}\text{C}$ to $-25\text{ }^{\circ}\text{C}$. The reason for the slight difference in COP was that the lower ambient temperature led to a higher $LMTD_{cond}$. So according to Eq. (13) and Eq. (15), the airflow rate increased, and, correspondingly, the refrigerant mass flow rate reduced a little. Hence, the compressor power consumption also decreased. Due to the unchanged heating capacity and increased air mass flow rate, when the ambient temperature varied in the range of $5\text{ }^{\circ}\text{C}$ and $-25\text{ }^{\circ}\text{C}$, the outlet air temperature decreased, as illustrated in the diagram in the bottom-right corner of Fig. 12. Fig. 12 also shows the comparison with the performance of other EV heat pump systems. Wang et al. [16] and Dong et al. [17] both studied the performance of the CO_2 EV heat pump system. Although Wang's system could provide a higher heating capacity than the proposed system in this article, it had the lowest COP among the four highlighted systems in Fig. 12. Additionally, even though the proposed system using R134a as a working refrigerant, it provided both higher COP and heating capacity than Dong's CO_2 heat pump system under the same ambient temperature.

Fig. 13 shows the variation of outlet air temperature and system COP in terms of condenser coolant inlet temperature. The results show that the COP increased with the increase of evaporator coolant inlet temperature while the outlet air temperature experienced the opposite trend. The reason could be attributed to the necessity of reducing refrigerant mass flow rate. In order to keep the heat balance between the coolant side and refrigerant side of plate heat exchanger, the model first adjusted the mass flow rate of the coolant as the evaporator coolant inlet temperature increased. The reduction of coolant mass flow rate needed an increase of ΔT_{cl} in Eq. (13) as a compensation. Therefore, the coolant outlet temperature further decreased to guarantee it could abstract all the waste heat from the fuel cell stack. Based on the temperature difference assumption between the coolant outlet temperature and evaporating temperature, the evaporating temperature declined as well.

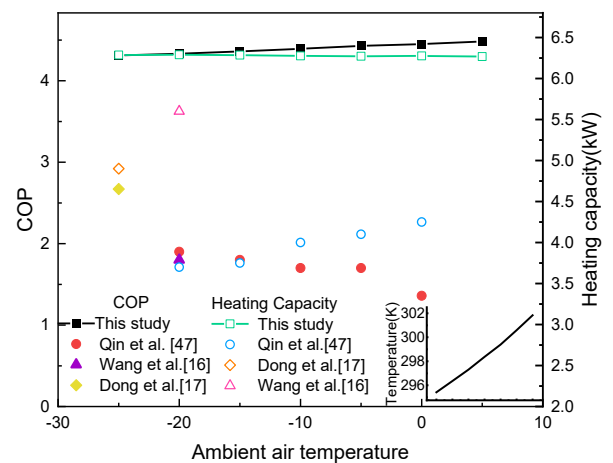


Fig. 12. Impact of ambient air temperature on COP and outlet air temperature and comparison with previous publications ($C_{dch} = 0.237$, $T_{cl_eva_inlet} = 30\text{ }^{\circ}\text{C}$, $I_{FC} = 220\text{A}$, $T_{sub} = 0\text{ }^{\circ}\text{C}$).

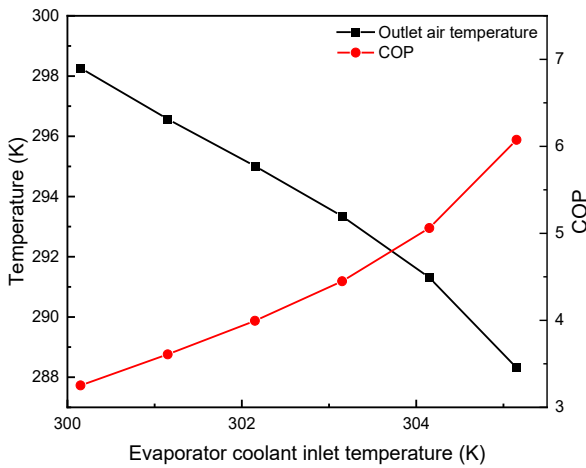


Fig. 13. Influence of condenser coolant inlet temperature on outlet air temperature and COP ($C_{dch} = 0.237$, $T_{amb} = 0\text{ }^\circ\text{C}$, $I_{FC} = 220\text{A}$, $T_{sub} = 0\text{ }^\circ\text{C}$).

Refrigerant mass flow rate, as a key parameter, directly affected the heat exchanger heat transfer coefficient on the refrigerant side. It was also reduced to ensure the conversion of energy. As a result, the COP is augmented due to the reduction of compressor power consumption under the same heat capacity. Lower refrigerant mass flow rate led to a lower compressing ratio and discharging temperature which also reduced the temperature difference between the condenser and the external environment. Therefore, the air mass flow rate increased and caused a decrease in outlet air temperature. Overall, the evaporator coolant inlet temperature should be carefully controlled because it has a significant influence on COP and outlet air temperature.

4.4. Equivalent effective battery capacity and payback duration

Due to the limited space in the vehicle, a fuel cell backup system would sacrifice some space that was previously used for the battery pack. After the battery pack was scaled down, the capacity of the battery pack also declined correspondingly. The equivalent battery capacity in the proposed system could be divided into three parts, the fuel cell supplement element, the heat pump consumption part and the initial electricity storage capacity of the remaining battery pack. The remaining portion of the initial battery capacity, after being consumed by the heating system and the replenishment from the fuel cell stack was defined as the EEBC in Eq. (41) which can be used for driving. The variations of those three energy elements over operating hours were displayed in Fig. 14. With the operating time increased, the heat pump power consumption and fuel cell power supplement were continuously increasing. Meanwhile, the initial part of the battery capacity was decreasing but the EEBC was increasing. Fig. 15. shows the EEBC that could be used for driving with respect to the heat pump system running hours. The electric vehicle air source heat pump (EVASHP) was selected from Ref. [16], which proved that the pump can provide around 6 kW heat. The working condition in Fig. 15 was at $-20\text{ }^\circ\text{C}$ ambient temperature, and the heating demand was 5.986 kW. In comparison, the proposed system has a COP of 6, while the COP of EVASHP, as described in previous work is only 1.8. [16]. The efficiency of the PTC heater was assumed as 0.9 and the battery initial SOC was assumed as 0.8 to avoid overcharging. It can be concluded that the longer the operating hours the higher the benefit achievable by the proposed FCBEV heat pump-assisted thermal management system. When the operating period was less than 2 h, the suggested system in this research could only provide the lowest EEBC compared to the EVASHP system and PTC system, as the charging current from the fuel cell stack could not supply equivalent power as sacrificed battery capacity. Hence the electricity that could be used for driving is 17.9% lower than the EVASHP system and 11.4%

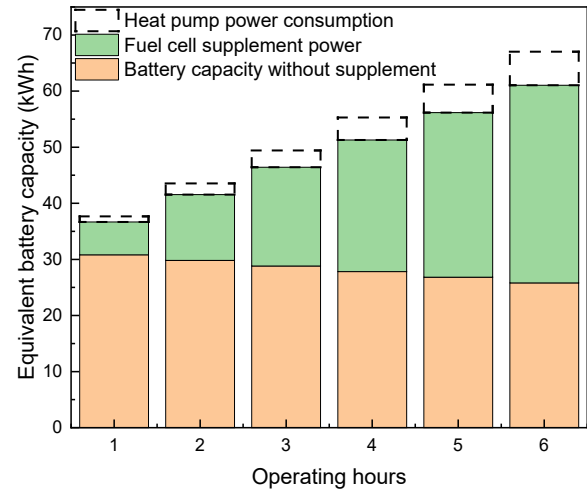


Fig. 14. Variation of battery capacity of the proposed system over operating time.

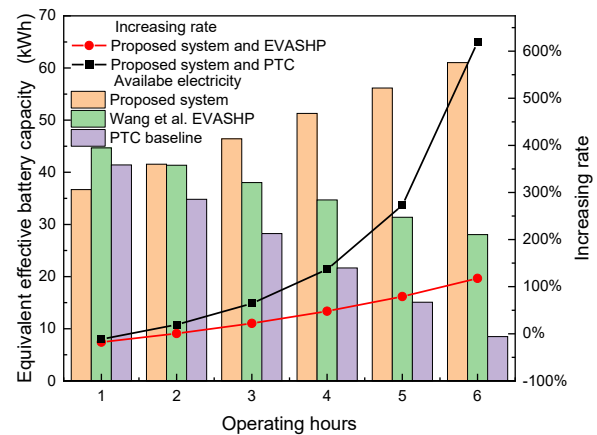


Fig. 15. Comparison of the amount of electricity that can be used for driving and increasing rate for proposed system, EVASHP system, and PTC system.

lower than the PTC system. However, the proposed system in this study displayed significant advantages when the operating period was greater than 2 hours. For example, when the operating period was 5 hours, the available power for driving is increased by 90% compared to EVASHP and 300% compared to the PTC system. It should be mentioned that the EVASHP selected for comparison did not consider the frosting and defrosting phenomenon on its OHX which normally dramatically affects the EVASHP's COP. In contrast, the proposed fuel cell backup heat pump assisted BEV thermal management system recovered the heat from the fuel cell coolant and battery pack and did not suffer from such impact. Therefore, the proposed system has a crucial advantage compared to the current existing EVASHP system, but crucial attention should be paid to the amount of H_2 charging within one charging cycle. It is necessary to store on-board H_2 that can supply power to the battery pack for at least 2 hours. However, this does not simply mean that more on-board hydrogen storage results in better performance, because issues such as hydrogen storage space and cost also should be considered.

Assuming the setting heat pump assisted FCBEV system runs for 4 h with a 51.3kWh equivalent battery capacity within one charging time as the target case. The price of H_2 , 5 kW fuel cell stack and electricity price are concluded in Table 6. The price of the 5 kW fuel cell stack also includes the cost of sales. Fig. 16 represents an economic analysis of each system with the same battery capacity available for driving. For the

proposed system in this study, the cost under the selected case is £10.40 for a single charging cycle while EVASHP system [16] and PTC system is respectively £13.80 and £19.20 which means that the suggested system could save around 16.4% and 39.5% within one charging cycle. Moreover, the payback duration was calculated based on the 5 kW fuel cell stack. The result in Fig. 16. shows it will take 10,500 charging times to earn back the initial cost of the fuel cell stack. However, the cost of the fuel cell stack and price of hydrogen fuel will be further improved with increasing production requirements and infrastructure development and, consequently, the pay pack duration will reduce sharply in the future.

5. Conclusions

A fuel cell backup and heat pump assisted FCBEVs thermal management system was proposed to improve the performance of BEVs under extreme cold weather from both efficiency and economic perspectives. Numerical models for fuel cell, heat exchangers and compressor were developed and validated by using published experimental data. The impacts of different vital operating conditions and the degree of improvement in EEBC were concluded and discussed. Based on the simulation results, the following conclusions were drawn.

- The COP increased with the increase of fuel cell stack output current. Contrarily, the outlet air temperature would reduce as the need for increasing the air mass flow rate occurred. When FC current output is greater than 217A, the outlet air temperature started lower than the FC coolant outlet temperature.
- The battery discharging rate had a similar impact on COP compared to fuel cell current output. However, the inlet vapour quality difference between the FC and battery would be narrowed with a decrease in battery discharging rate.
- The COP showed a decreasing trend while introducing a larger subcooling degree. But the operating range and outlet temperature increased correspondingly. Hence, when the size of components is fixed, regulating the subcooling degree is a useful way to fulfil different ranges or higher air temperature requirements.
- Different from ASHP, the air temperature has no significant effect on the proposed system. When the ambient temperature varied from 5 °C to -25 °C, the COP only decreased by 3.7%
- Evaporator coolant inlet temperature had the greatest influence on the COP among the defined independent variables. When the evaporator coolant inlet temperature increased 5 °C from 30 °C to 35 °C, the COP could increase by 87%.
- The COP of the proposed system is 2.3 times that of a EVASHP system at -20 °C. Heating capacity fluctuated by only 0.3%, while the mentioned counterpart fluctuated by 14.8% when the air temperature dropped from 0 °C to -20 °C.
- When the operating period was greater than 2 h, the increasing rate of effective battery capacity compared to the traditional heat pump thermal management system in BEV increased dramatically, even meeting 79.04% when the operating period was 4 h.
- The proposed system had the lowest cost for each H₂ and battery charging time. The payback duration was 10,500 charging cycles.

Table 6
Components cost for the proposed system.

| Components | Prices |
|--|----------------------------|
| H ₂ [48] | 3.26 (£/kg) |
| Electricity [49] | 0.19 (£/kg) |
| 5 kW fuel cell stack(10000 units/year)[50] | Manufacturing 21068.94 (£) |
| | CHP hardware |
| | BOP hardware |
| | Sales (50%) |

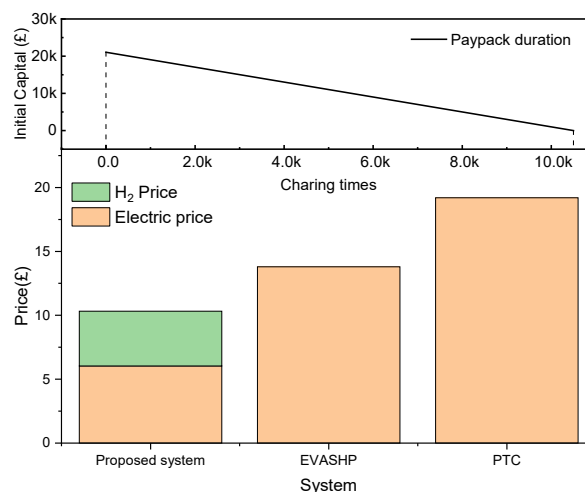


Fig. 16. Economic analysis for each system and payback cycle for the proposed system under 4 h of operating period.

6. Outlook and future perspectives

The study demonstrated that the proposed fuel cell battery electric vehicle energy system integrating with a heat pump technology thermal management system could always provide a higher COP than a conventional R134a EVs' air source heat pump and even higher than a CO₂ air source heat pump. Subcooling degrees could extend the operating range to a certain extent. Hence, optimizing the subcooling degree may be a beneficial control strategy to cover a wider operating range without changing the components. The plate heat exchanger used in this work may have some impacts on the variation rate of the coolant and refrigerant mass flow rate and the evaporating temperature. Further research could focus on the effect of the plate gap on the system performance by influencing the temperature difference between coolant temperature and evaporating temperature. Moreover, the air mass flow rate in this work could not be adjusted manually as it is a dependent variable in the proposed system. Consequently, further study could also modify the current system to improve the system's practicality. Finally, the work was a stable simulation which did not consider the impact of the SOC and temperature of the battery pack and fuel cell stack. Further work could analyse the system from a dynamic perspective and link it to the practical driving cycle. Meanwhile, the fuel cell stack current output and battery discharging rate was considered independently in this present work. However, due to the limit of capacity, these components should change correspondingly in dynamic simulation.

CRediT authorship contribution statement

Nan Zhang: Writing – original draft, Formal analysis, Methodology, Software, Validation. **Yiji Lu:** Conceptualization, Writing – review & editing, Supervision. **Sambhaji Kadam:** Writing – review & editing, Methodology, Validation. **Zhibin Yu:** Conceptualization, Methodology, Supervision.

Declaration of Competing Interest

The authors declare that they have no known competing financial interests or personal relationships that could have appeared to influence the work reported in this paper.

Data availability

Data will be made available on request.

Acknowledgements

The authors would like to thank the support of EPSRC Decarbonisation of Heating and Cooling (EP/T022701/1) and the ETP/Transport Scotland Industry Engagement Fund. This work was also funded by the University of Glasgow Studentship and China Scholarship Council (CSC) (202008230188). Also, thanks to the high-quality proofreading service provided by Ms Lisa Smeaton <https://www.linkedin.com/in/lisa-smeaton-39357b19a/>.

References

- [1] Canals Casals L, Martinez-Laserna E, Amante García B, Nieto N. Sustainability analysis of the electric vehicle use in Europe for CO₂ emissions reduction. *J Clean Prod* 2016;127:425–37.
- [2] Smith P, Beaumont L, Bernacchi CJ, Byrne M, Cheung W, Conant RT, et al. Essential outcomes for COP26. *Glob Chang Biol* 2022;28:1–3.
- [3] Zhang Z, Li W, Zhang C, Chen J. Climate control loads prediction of electric vehicles. *Appl Therm Eng* 2017;110:1183–8.
- [4] Shin YH, Sim S, Kim SC. Performance Characteristics of a Modularized and Integrated PTC Heating System for an Electric Vehicle. *Energies* 2016;9:18.
- [5] Zhang Z, Wang D, Zhang C, Chen J. Electric vehicle range extension strategies based on improved AC system in cold climate – A review. *Int J Refrig* 2018;88:141–50.
- [6] Higuchi Y, Kobayashi H, Shan Z, Kuwahara M, Endo Y, Nakajima Y. Efficient heat pump system for PHEV/BEV. *SAE Technical Paper*; 2017.
- [7] Marcotte M, Grabowski S. 16 - Minimising energy consumption associated with drying, baking and evaporation. In: Klemes J, Smith R, Kim J-K, editors. *Handbook of Water and Energy Management in Food Processing*. Woodhead Publishing; 2008. p. 481–522.
- [8] Qin F, Shao S, Tian C, Yang H. Experimental Investigation on Heating Performance of Heat Pump for Electric Vehicles in Low Ambient Temperature. *Energy Procedia* 2014;61:726–9.
- [9] Zhang Z, Li W, Shi J, Chen J. A Study on Electric Vehicle Heat Pump Systems in Cold Climates. *Energies* 2016;9:881.
- [10] Qin F, Zhang G, Xue Q, Zou H, Tian C. Experimental investigation and theoretical analysis of heat pump systems with two different injection portholes compressors for electric vehicles. *Appl Energy* 2017;185:2085–93.
- [11] Choi YU, Kim MS, Kim GT, Kim M, Kim MS. Performance analysis of vapor injection heat pump system for electric vehicle in cold startup condition. *Int J Refrig* 2017;80:24–36.
- [12] Jung J, Jeon Y, Cho W, Kim Y. Effects of injection-port angle and internal heat exchanger length in vapor injection heat pumps for electric vehicles. *Energy* 2020;193.
- [13] Kwon C, Kim MS, Choi Y, Kim MS. Performance evaluation of a vapor injection heat pump system for electric vehicles. *Int J Refrig* 2017;74:138–50.
- [14] Qin F, Liu H, Zou H, Chen D, Tian C. Experiment Investigation and Control Strategies on Two-Phase Refrigerant Injection Heat Pump System for Electric Vehicle in Start-up Stage. *J Therm Sci* 2021;30:828–39.
- [15] Li W, Liu R, Liu Q, Liu Y, Wang D, Xia S, et al. Upstream and downstream injection effects on R134a economized vapor injection heat pump system at low temperatures for electric vehicles. *Int J Refrig* 2020;120:1–11.
- [16] Wang D, Yu B, Li W, Shi J, Chen J. Heating performance evaluation of a CO₂ heat pump system for an electrical vehicle at cold ambient temperatures. *Appl Therm Eng* 2018;142:656–64.
- [17] Junqi D, Yibiao W, Shiwei J, Xianhui Z, Linjie H. Experimental study of R744 heat pump system for electric vehicle application. *Appl Therm Eng* 2021;183.
- [18] Shen M, Gao Q. System simulation on refrigerant-based battery thermal management technology for electric vehicles. *Energy Convers Manage* 2020;203.
- [19] Varma M, Jaybhay S, Kadam K, Venu S, Kulkarni S, Kapoor S. Cabin and Battery Cooling Performance Trade-off in an Electric Vehicle. *SAE Technical Paper Series*; 2020.
- [20] Ma J, Sun Y, Zhang S, Li J, Li S. Experimental study on the performance of vehicle integrated thermal management system for pure electric vehicles. *Energy Convers Manage* 2022;253:115183.
- [21] Tian Z, Gu B, Gao W, Zhang Y. Performance evaluation of an electric vehicle thermal management system with waste heat recovery. *Appl Therm Eng* 2020;169.
- [22] Jeffs J, McGordon A, Picarelli A, Robinson S, Tripathy Y, Widanage WD. Complex Heat Pump Operational Mode Identification and Comparison for Use in Electric Vehicles. *Energies* 2018;11:2000.
- [23] Ding P, Wang Z, Wang Y, Li K. A distributed multiple-heat source staged heating method in an electric vehicle. *Renew Energy* 2020;150:1010–8.
- [24] Ehrenstein M, Galán-Martín Á, Tulus V, Guillén-Gosálbez G. Optimising fuel supply chains within planetary boundaries: A case study of hydrogen for road transport in the UK. *Appl Energy* 2020;276:115486.
- [25] Xu J, Zhang C, Fan R, Bao H, Wang Y, Huang S, et al. Modelling and control of vehicle integrated thermal management system of PEM fuel cell vehicle. *Energy* 2020;199.
- [26] Lee H, Lee D, Kim Y. Heating performance of a coolant-source heat pump using waste heat from stack and electric devices in fuel cell electric vehicles under cold conditions. *Energy Convers Manage* 2022;252:115092.
- [27] Albayati I, Ali R, Calay R. Modelling and Examining Open Circuit Voltage for PEM Fuel Cells. *J Electr Eng* 2013;13:140–6.
- [28] Mann RF, Amphlett JC, Hooper MA, Jensen HM, Peppley BA, Roberge PR. Development and application of a generalised steady-state electrochemical model for a PEM fuel cell. *J Power Sources* 2000;86:173–80.
- [29] Khan M, Iqbal M. Dynamic modeling and simulation of a small wind-fuel cell hybrid energy system. *Renew Energy* 2005;30:421–39.
- [30] Saleh IMM, Ali R, Zhang H. Simplified mathematical model of proton exchange membrane fuel cell based on horizon fuel cell stack. *J Mod Power Syst Clean Energy* 2016;4:668–79.
- [31] Wang Y, Wang C-Y. Modeling polymer electrolyte fuel cells with large density and velocity changes. *J Electrochem Soc* 2005;152:A445.
- [32] Dicks A, Rand D. *Fuel Cell Systems Explained* 2018.
- [33] Liso V, Nielsen MP, Kær SK, Mortensen HH. Thermal modeling and temperature control of a PEM fuel cell system for forklift applications. *Int J Hydrogen Energy* 2014;39:8410–20.
- [34] Şefkat G, Özel MA. Experimental and numerical study of energy and thermal management system for a hydrogen fuel cell-battery hybrid electric vehicle. *Energy* 2022;238.
- [35] Mahamud R, Park C. Reciprocating air flow for Li-ion battery thermal management to improve temperature uniformity. *J Power Sources* 2011;196:5685–96.
- [36] Liu G, Ouyang M, Lu L, Li J, Han X. Analysis of the heat generation of lithium-ion battery during charging and discharging considering different influencing factors. *J Therm Anal Calorim* 2014;116:1001–10.
- [37] TRANSPORTATION USDO. New car assessment program (NCAP) FMVSS NO. 305 incandent test. 2013.
- [38] Incropera FP, DeWitt DP. *Fundamentals of Heat and Mass*. Transfer: Wiley; 2002.
- [39] Donowski V. Theoretical investigation of the evaporation heat transfer coefficient of refrigerant R-134a in a plate heat exchanger. *Rochester Institute of Technology*; 1999.
- [40] Yan YY, Lin TF. Evaporation Heat Transfer and Pressure Drop of Refrigerant R-134a in a Plate Heat Exchanger. *J Heat Transfer* 1999;121:118–27.
- [41] Dobson MK, Chato JC. Condensation in Smooth Horizontal Tubes. *J Heat Transfer* 1998;120:193–213.
- [42] Wallis GB. Discussion: “Estimation of Steady-State Steam Void-Fraction by Means of the Principle of Minimum Entropy Production” (Zivi, S. M., 1964, ASME J. Heat Transfer, 86, pp. 247–251). *Journal of Heat Transfer*. 1964;86:252.
- [43] Cuevas C, Fonseca N, Lemort V. Automotive electric scroll compressor: Testing and modeling. *Int J Refrig* 2012;35:841–9.
- [44] Tian Z, Gan W, Zhang X, Gu B, Yang L. Investigation on an integrated thermal management system with battery cooling and motor waste heat recovery for electric vehicle. *Appl Therm Eng* 2018;136:16–27.
- [45] Ríos GM, Schirmer J, Gentner C, Kallo J. Efficient thermal management strategies for cold starts of a proton exchange membrane fuel cell system. *Appl Energy* 2020;279:115813.
- [46] Luo M, Zhang J, Zhang C, Chin CS, Ran H, Fan M, et al. Cold start investigation of fuel cell vehicles with coolant preheating strategy. *Appl Therm Eng* 2022;201:117816.
- [47] Qin F, Xue Q, Albarracín Velez GM, Zhang G, Zou H, Tian C. Experimental investigation on heating performance of heat pump for electric vehicles at –20 °C ambient temperature. *Energy Convers Manage* 2015;102:39–49.
- [48] Ajanovic A, Glatt A, Haas R. Prospects and impediments for hydrogen fuel cell buses. *Energy* 2021;235:121340.
- [49] Labor DoLLUSDo. Average energy prices for the United States, regions, census divisions, and selected metropolitan areas. United States government; 2022.
- [50] Institute BM. Manufacturing Cost Analysis of 1, 5, 10 and 25 kW Fuel Cell Systems for Primary Power and Combined Heat and Power Applications. In: *energy USDO*, editor; 2017.